Eur. Phys. J. A (2025) 61:73
https://doi.org/10.1140/epja/s10050-025-01493-w

THE EUROPEAN PHYSICAL JOURNAL A

Regular Article - Theoretical Physics

On the influence of nuclear deformation in the elastic scattering of polarized electrons

D. H. Jakubassa-Amundsen[a]

Mathematics Institute, University of Munich, Theresienstrasse 39, 80333 Munich, Germany

Received: 11 November 2024 / Accepted: 16 January 2025

Communicated by Arnau Rios Huguet

Abstract Elastic electron scattering from deformed nuclei is described within the distorted-wave Born approximation (DWBA) by employing charge densities which reflect, respectively, the prolate and oblate shapes of the target nucleus. Clear evidence for the shape dependence of the differential cross section and of the electronic spin asymmetry is found at scattering angles in the vicinity of the first diffractive cross section minimum. As an example, results for the ^{27}Al nucleus at collision energies between 150 and 500 MeV are provided.

1 Introduction

The study of nuclear deformation provides information on the nature and the forces of the nuclear many-body system [1]. In particular, it serves to understand the spectra of a deformed nucleus or its decay if it is unstable.

In a recent paper [2] the elastic scattering of unpolarized electrons from a series of polarized nuclei with a quadrupole deformed ground state was considered. Within the framework of the plane-wave Born approximation (PWBA), where the differential cross section for unpolarized targets is expressed in terms of an incoherent sum over charge and magnetic form factors of different multipolarities, the use of a polarized target results in coherent sums of these form factors. It was demonstrated that the corresponding interference terms lead to a significant difference between the prolate and oblate shapes of the nuclei.

In the present work it is shown within the DWBA formalism that the prolate-oblate difference manifests itself, even for unpolarized collision partners, in the differential scattering cross section. It is also visible in the spin asymmetry of electrons polarized perpendicular to the scattering plane. In the forward hemisphere the $L = 0$ form factor (corresponding to the spherical part of the nuclear charge distribution) is dominant, while at large scattering angles the magnetic form factors become important. Therefore the influence of the $L = 2$ form factor which is sensitive to the quadrupole deformation of the nuclear charge distribution will only be visible at intermediate angles when the cross section resulting from potential scattering has a diffraction minimum. The ^{27}Al nucleus has been chosen since the first excited (oblate) state is in energy close to the (prolate) ground state, such that the two respective transition densities, as provided in [2], can to a good approximation be used to distinguish between prolate and oblate ground states.

The paper is organized as follows. Section 2 gives an outline of the theory for polarized electron-nucleus scattering, where it is also shown that the differential cross section separates into its multipole constituents in case of unpolarized nuclei. The transition densities are discussed in Sect. 3, and Sect. 4 provides the nuclear shape studies, including the influence of additional nuclear polarization. The conclusion is drawn in Sect. 5. Atomic units ($\hbar = m = e = 1$) are used unless indicated otherwise.

2 Theory

A detailed description of elastic electron scattering within the partial-wave approach, using the phase-shift analysis for potential (L = 0) scattering and the distorted-wave Born approximation (DWBA) for the higher multipole transitions, is provided in [3,4]. In short, the differential cross section for scattering an electron with momentum $\boldsymbol{k}_i$, total energy E_i and spin polarization vector $\boldsymbol{\zeta}_i$ from an unpolarized nucleus with spin J_i into the solid angle $d\Omega$ is given by (see, e.g. [5])

---

[a] e-mail: dj@mathematik.uni-muenchen.de (corresponding author)

$$\frac{d\sigma}{d\Omega}(\boldsymbol{\zeta}_i, \boldsymbol{\zeta}_f) = \frac{k_f}{k_i}\,\frac{1}{f_{\text{rec}}}\,\frac{1}{2J_i+1}\,S_{fi},$$

$$S_{fi} = \sum_{M_f, M_i}\Bigg| A_{fi}^{\text{coul}}\delta_{M_i,M_f} + \left(4\pi^3\frac{E_iE_f}{c^2}\right)^{\frac{1}{2}} \times \left[A_{fi}^{ch}(M_i,M_f) + A_{fi}^{\text{mag}}(M_i,M_f)\right]\Bigg|^2, \tag{2.1}$$

where $\boldsymbol{k}_f$, E_f and $\boldsymbol{\zeta}_f$ are, respectively, momentum, total energy and spin polarization of the scattered electron. A sum over the final polarization M_f and an average over the initial polarization M_i of the nucleus is included. Recoil is accounted for by the prefactor f_{rec} [6] and by employing a reduced collision energy $E = \sqrt{(E_i - c^2)(E_f - c^2)}$ for the Coulombic scattering amplitude A_{fi}^{coul}. This scattering amplitude is identified with the amplitude $f_e(\boldsymbol{\zeta}_i, \boldsymbol{\zeta}_f, k_i, \theta)$ for potential scattering from the spherical part of the nuclear charge distribution, where θ is the scattering angle. The multipole decomposition of the nuclear charge distribution ϱ is commonly defined by

$$\varrho(\boldsymbol{r}_N) = \sum_{L\ge 0}\varrho_L(r_N)\,Y_{L0}(\hat{r}_N) = \sum_{L\ge 0}\sqrt{\frac{2L+1}{4\pi}}\,\varrho_L(r_N)\,P_L(\cos\theta), \tag{2.2}$$

where Y_{LM} is a spherical harmonic function and P_L a Legendre polynomial [7]. A similar decomposition holds for the nuclear current distribution $\boldsymbol{j}$ [6]. The density distributions ϱ and $\boldsymbol{j}$ are determined from nuclear models.

The charge scattering amplitude is defined by

$$A_{fi}^{ch}(M_i,M_f) = -\frac{1}{c}\int d\boldsymbol{r}_N d\boldsymbol{r}_e \left(\psi_f^{(\sigma_f)+}(\boldsymbol{r}_e)\;\psi_i^{(\sigma_i)}(\boldsymbol{r}_e)\right) \times \frac{1}{|\boldsymbol{r}_e - \boldsymbol{r}_N|}\,\varrho_{fi}(\boldsymbol{r}_N)$$

$$\varrho_{fi}(\boldsymbol{r}_N) = \sum_{\substack{L>0\\ even, M}} (J_iM_iLM|\,J_iM_f)\varrho_L(r_N)Y_{LM}(\hat{\boldsymbol{r}}_N), \tag{2.3}$$

where $\psi_i^{(\sigma_i)}$ and $\psi_f^{(\sigma_f)}$ denote the initial, respectively final, electronic scattering states with spin projection σ_i and σ_f. The nuclear charge transition amplitude ϱ_{fi} is represented in terms of the charge densities ϱ_L for each contributing multipole.

The magnetic scattering amplitude A_{fi}^{mag} is obtained from

$$A_{fi}^{\text{mag}}(M_i,M_f) = \frac{1}{c}\int d\boldsymbol{r}_N d\boldsymbol{r}_e \left(\psi_f^{(\sigma_f)+}(\boldsymbol{r}_e)\,\boldsymbol{\alpha}\,\psi_i^{(\sigma_i)}(\boldsymbol{r}_e)\right) \times \frac{\overset{\leftrightarrow}{I}}{|\boldsymbol{r}_e - \boldsymbol{r}_N|}\,\boldsymbol{j}_{fi}(\boldsymbol{r}_N), \tag{2.4}$$

where $\boldsymbol{\alpha}$ is a vector of Dirac matrices and $\overset{\leftrightarrow}{I}$ is the dyadic unit matrix. The nuclear current transition amplitude $\boldsymbol{j}_{fi}$ is likewise multipole expanded in terms of the magnetic densities J_{LL},

$$\boldsymbol{j}_{fi}(\boldsymbol{r}_N) = -i\sum_{\substack{L>0\\ odd, M}} (J_iM_iLM|J_iM_f)J_{LL}(r_N)\boldsymbol{Y}_{LL}^{M}(\hat{\boldsymbol{r}}_N), \tag{2.5}$$

where $\boldsymbol{Y}_{LL}^{M}$ is a vector spherical harmonic. The restriction of the angular momentum sums in (2.3) and (2.5) is dictated by parity conservation and time reversal invariance [3,6]. Details of the evaluation of (2.3) and (2.4) can be found in [4,5]. In particular, the electronic radial integrals are performed numerically with the help of the complex-plane rotation method [8,9].

The densities ϱ_L and J_{LL} enter incoherently into the cross section (2.1), due to the sum over the nuclear magnetic quantum numbers M_i and M_f. For the charge multipoles $L = 0$ and $L = 2$ this was already predicted in early work [1]. Here we consider the general case and derive the respective formulas. The sum over M_i and M_f is written in the following way,

$$S_{fi} = (2J_i+1)\,|A_{fi}^{\text{coul}}|^2 + 2\,\text{Re}\Big\{A_{fi}^{\text{coul}*}\sum_{M_i}\Big[\tilde{A}_{fi}^{ch}(M_i,M_i) + \tilde{A}_{fi}^{\text{mag}}(M_i,M_i)\Big]\Big\} + \sum_{M_i,M_f}\Big[|\tilde{A}_{fi}^{ch}(M_i,M_f)|^2 + |\tilde{A}_{fi}^{\text{mag}}(M_i,M_f)|^2 + 2\,\text{Re}\{\tilde{A}_{fi}^{ch*}(M_i,M_f)\tilde{A}_{fi}^{\text{mag}}(M_i,M_f)\}\Big], \tag{2.6}$$

where the tilde abbreviates the multiplication of A_{fi}^{ch} and A_{fi}^{mag} with the prefactor $\left(4\pi^3\frac{E_iE_f}{c^2}\right)^{\frac{1}{2}}$.

We start by showing that the interference terms between A_{fi}^{coul}, A_{fi}^{ch} and A_{fi}^{mag} vanish. Suppressing M_i−independent factors, one has

$$\sum_{M_i}\tilde{A}_{fi}^{ch}(M_i,M_i) \sim \sum_{M_i}\varrho_{fi}(\boldsymbol{r}_N) = \sum_{\substack{L>0\\ even}}\sum_{M_i}(J_iM_iL\,0\,|\,J_iM_i)\,\varrho_L(r_N)\,Y_{L0}(\hat{\boldsymbol{r}}_N). \tag{2.7}$$

Upon multiplying by a Clebsch-Gordan coefficient which is unity, the sum over M_i is found to be [7]

$$\sum_{M_i}(J_iM_iL\,0\,|J_iM_i)(J_iM_i0\,0|\,J_iM_i) = \frac{2J_i+1}{\sqrt{2L+1}}\,\delta_{L0}, \tag{2.8}$$

singling out $L = 0$.

From (2.5) it follows that the factor (2.8) also occurs in $\sum_{M_i} \tilde{A}_{fi}^{\mathrm{mag}}(M_i, M_i)$. This proves that there is no interference between A_{fi}^{coul} and $\tilde{A}_{fi}^{ch}$ or $\tilde{A}_{fi}^{\mathrm{mag}}$, since $L > 0$ is mandatory for the latter two terms.

For the interference term between A_{fi}^{ch} and A_{fi}^{mag} one has, again suppressing all M_i- and M_f-independent factors [7],

$$\begin{aligned}\sum_{M_i,M_f} \tilde{A}_{fi}^{ch*}(M_i, M_f)\tilde{A}_{fi}^{\mathrm{mag}}(M_i, M_f) &\sim \sum_{M_i,M_f} \varrho_{fi}^{*}(\boldsymbol{r}_N)\boldsymbol{j}_{fi}(\boldsymbol{r}'_N) \\ &\sim \sum_{L\,\mathrm{even}}\sum_{\lambda\,\mathrm{odd}}\sum_{M,\mu}\sum_{M_i,M_f} (J_i M_i L\, M\,|J_i M_f)(J_i M_i \lambda\, \mu|\, J_i M_f) \\ &= \sum_{L\,\mathrm{even}}\sum_{\lambda\,\mathrm{odd}}\sum_{M,\mu} \frac{2J_i+1}{\sqrt{2L+1}\sqrt{2\lambda+1}}\,\delta_{\lambda L}\,\delta_{\mu M} \;=\; 0. \end{aligned} \tag{2.9}$$

It remains to treat the quadratic terms with $L > 0$ in (2.6). However, they contain the same product of Clebsch-Gordan coefficients as appears in (2.9), such that

$$\begin{aligned}\sum_{M_i,M_f} \varrho_{fi}^{*}(\boldsymbol{r}_N)\,\varrho_{fi}(\boldsymbol{r}'_N) \;=\; (2J_i+1)\sum_{LM} \\ \times\, \varrho_L(r_N)\, Y_{LM}^{*}(\hat{\boldsymbol{r}}_N)\, \varrho_L(r'_N)\, Y_{LM}(\hat{\boldsymbol{r}}'_N)\,\frac{1}{2L+1}\end{aligned} \tag{2.10}$$

and

$$\begin{aligned}\sum_{M_i,M_f} \boldsymbol{j}_{fi}^{+}(\boldsymbol{r}_N)\,\boldsymbol{j}_{fi}(\boldsymbol{r}'_N) \;=\; (2J_i+1)\sum_{LM} J_{LL}(r_N) \\ \times \boldsymbol{Y}_{LL}^{*M}(\hat{\boldsymbol{r}}_N)\, J_{LL}(r'_N)\, \boldsymbol{Y}_{LL}^{M}(\hat{\boldsymbol{r}}'_N)\,\frac{1}{2L+1}.\end{aligned} \tag{2.11}$$

Therefore the cross section (2.1) reduces to

$$\begin{aligned}\frac{d\sigma}{d\Omega}(\boldsymbol{\zeta}_i, \boldsymbol{\zeta}_f) \;=\; \frac{k_f}{k_i}\,\frac{1}{f_{\mathrm{rec}}}\Bigg\{|A_{fi}^{\mathrm{coul}}|^2 + \left(4\pi^3\,\frac{E_i E_f}{c^2}\right) \\ \left[\sum_{L\mathrm{even}} W_L^{ch} \;+\; \sum_{L\mathrm{odd}} W_L^{\mathrm{mag}}\right]\Bigg\}\end{aligned} \tag{2.12}$$

with

$$\begin{aligned}W_L^{ch} \;=& \frac{1}{c^2}\,\frac{1}{2L+1}\;\sum_M \Bigg|\int d\boldsymbol{r}_e d\boldsymbol{r}_N \left(\psi_f^{(\sigma_f)+}(\boldsymbol{r}_e)\psi_i^{(\sigma_i)}(\boldsymbol{r}_e)\right) \\ &\times\, \frac{1}{|\boldsymbol{r}_e - \boldsymbol{r}_N|}\varrho_L(r_N) Y_{LM}(\hat{\boldsymbol{r}}_N)\Bigg|^2\end{aligned} \tag{2.13}$$

and

$$\begin{aligned}W_L^{\mathrm{mag}} \;=& \frac{1}{c^2}\,\frac{1}{2L+1}\sum_M \Bigg|\int d\boldsymbol{r}_e\, d\boldsymbol{r}_N \\ &\times \left(\psi_f^{(\sigma_f)+}(\boldsymbol{r}_e)\,\boldsymbol{\alpha}\,\psi_i^{(\sigma_i)}(\boldsymbol{r}_e)\right)\,\frac{\overset{\leftrightarrow}{I}}{|\boldsymbol{r}_e - \boldsymbol{r}_N|}\,J_{LL}(r_N)\,\mathbf{Y}_{LL}^{M}(\hat{\boldsymbol{r}}_N)\Bigg|^2.\end{aligned} \tag{2.14}$$

The first summand in (2.12) defines the Coulombic cross section $\frac{d\sigma_{\mathrm{coul}}}{d\Omega}$. Although (2.12) manifests the incoherent summation of the three contributions to the cross section (such that the signs of A_{fi}^{ch} and A_{fi}^{mag} play no role), neither W_L^{ch} nor W_L^{mag} can be expressed in terms of squared form factors unless the electron is described by plane waves.

However, the PWBA is not suited for a quantitative study of the deformation effects. The reason is that the scattering eigenstates ψ_i and ψ_f (in contrast to the plane waves in PWBA) do not allow for a separate treatment of the electronic and nuclear matrix elements inherent in W_L^{ch} or W_L^{mag}. Hence relative phases become important, and the zeros of the form factors are smeared out in DWBA. Since the prolate-oblate difference is basically observable in the diffraction minima where nevertheless the $L = 0$ contribution is contained in the measurements, PWBA will enhance this shape difference by up to a factor of two as compared to DWBA, even for a target as light as aluminum.

3 Transition densities

The nucleus ^{27}Al has spin $J_i = \frac{5}{2}$, such that from $0 \leq L \leq 2J_i = 5$ one has $L = 2$ and 4 for the charge transitions and $L = 1, 3, 5$ for the magnetic transitions. The ground-state charge density ϱ_0, from which the nuclear potential is generated in order to obtain A_{fi}^{coul} or the electronic scattering states ψ_i and ψ_f, is taken in the form of a Fourier-Bessel expansion as tabulated in [10]. The states ψ_i and ψ_f are solutions to the Dirac equation. They are obtained with the help of the Fortran code RADIAL by Salvat et al. [11]. The densities ϱ_L and J_{LL} are calculated from the respective form factors F_L^c and F_L^{tm}, provided in [12], with the help of the transformation formula

$$\begin{pmatrix}\varrho_L(r) \\ J_{LL}(r)\end{pmatrix} \;=\; \frac{2}{\pi}\int_0^\infty q^2 dq\; j_L(qr)\begin{pmatrix}F_L^c(q) \\ F_L^{tm}(q)\end{pmatrix} \tag{3.1}$$

where j_L is a spherical Bessel function. In particular, the asymptotic properties of the charge and transverse magnetic form factors, $F_L \sim q^L$ for $q \to 0$ and $F_L \sim e^{-b^2q^2/4}$ for $q \to \infty$ with the oscillator length $b = 1.784$ fm for ^{27}Al, were used (after transforming from the effective momentum transfer q_{eff} [12] to q).

Figure 1a displays the charge densities ϱ_0, ϱ_2 and ϱ_4 as a function of the nuclear coordinate. In Fig. 1b the magnetic density distributions are shown. It is seen that for $r_N \gtrsim 2$ fm, J_{55} is largely dominating.

For obtaining the differential scattering cross section for unpolarized collision partners, an average over the initial (σ_i) and a sum over the final (σ_f) spin projections of the electron has to be performed,

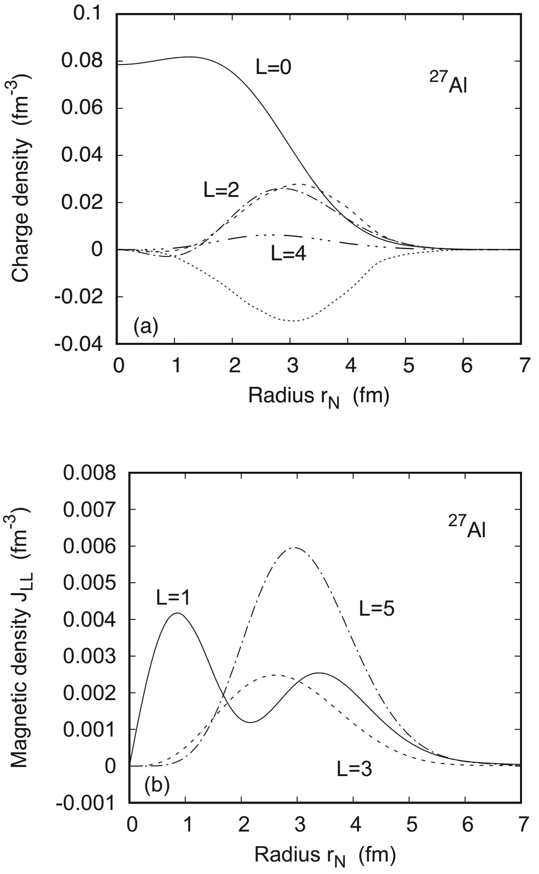

Fig. 1 Density distributions for the ^{27}Al ground state as a function of the nuclear coordinate r_N. **a** Charge densities ϱ_L for $L=0$ (——–), $L=2$ (– · – · –) and $L=4$ (– · · · – – · · · –) as obtained from [12]. Included are the $L=2$ density distributions from [2], multiplied by the factor $\sqrt{4\pi/5}$ (due to the omission [2] of the respective factor in (2.2)): – – – –, ϱ_2 (prolate), · · · · · · , ϱ_2 (oblate). **b** Magnetic densities J_{11} (——–), J_{33} (– – – –) and J_{55} (– · – · –) as obtained from [12]

$$\frac{d\sigma}{d\Omega} = \frac{1}{2} \sum_{\sigma_i,\sigma_f} \frac{d\sigma}{d\Omega}(\boldsymbol{\zeta}_i, \boldsymbol{\zeta}_f). \tag{3.2}$$

Figure 2 presents a comparison of the cross section with available experimental data on elastic electron scattering from ^{27}Al [13–15]. For the small-angle scattering at 500 MeV (Fig. 2a) the Coulombic ($L=0$) contribution $\frac{d\sigma_{\text{coul}}}{d\Omega}$ is mostly the dominant one. However, in the vicinity of the diffraction minima at 31° and 59° also the $L=2$ constituent comes into play. Near the second minimum even magnetic scattering is not negligible, while the $L=4$ contribution is small in the whole angular region, in concord with its tiny charge density (see Fig. 1a).

The results for large-angle scattering are shown in Fig. 2b in the energy region between 30 and 280 MeV. The experiments are performed at an angle of 180°, and the contribution from the $L=0$ potential scattering has been subtracted from the data. Therefore comparison is made with purely magnetic scattering (at $\theta = 178°$ where theory hardly changes with angle). While the low-energy data are well described by the $L=1$ constituent M_1, the cross section at high energies results basically from the $L=5$ contribution in concord with its dominant magnetic density (Fig. 1b). However, experiment is underpredicted by a factor of 2–3 for collision energies above 150 MeV.

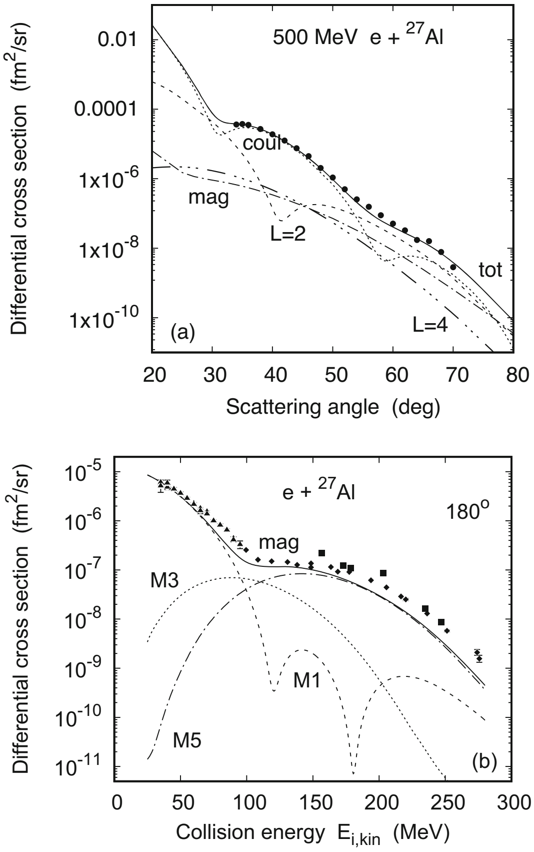

Fig. 2 Differential cross section $\frac{d\sigma}{d\Omega}$ for unpolarized electrons scattering from ^{27}Al **a** at 500 MeV as a function of scattering angle θ and **b** for backward scattering as a function of collision energy $E_{i,kin} = E_i - c^2$. In **a** the experimental data (●) from Li et al. [14] are compared with theory (———, including all $L \le 5$). Separately shown is the Coulombic phase-shift result (· · · · · ·) and the contributions from $L=2$ (– – – –) and $L=4$ (– · · · – – · · · –). Included is the summed magnetic contribution for $L \le 5$ (– · – · –). **b** Experimental data for magnetic scattering at 180° from Lapikás et al. (▲ [15]), from Li et al. (■ [13]) and from Hicks et al. (♦ as cited in [6]). Theoretical magnetic cross section at 178° including L=1,3,5 (———), as well as its constituents M_1 (– – – –), M_3 (· · · · · ·) and M_5 (– · – · –) corresponding, respectively, to $L = 1$, 3 and 5

4 Nuclear shape studies

In order to investigate the influence of the shape of deformed nuclei on the differential cross section and on the spin polarization of electron or nucleus, calculations are performed

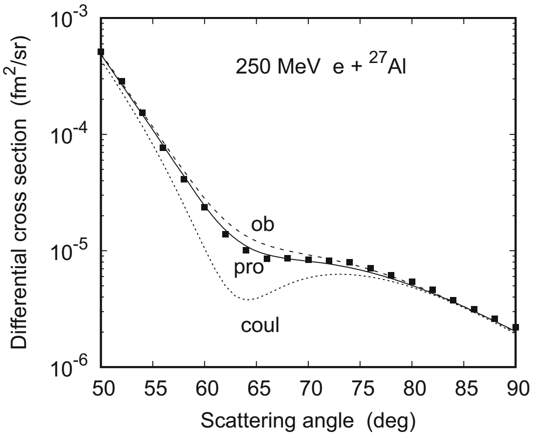

Fig. 3 Differential cross section $\frac{d\sigma}{d\Omega}$ for 250 MeV electrons scattering from ^{27}Al as a function of angle θ. Shown is the result, summed over L, in case of a prolate quadrupole density distribution (———) and for the oblate one (— — — —). Also shown is the result from potential scattering, i.e. $L = 0$ (· · · · · ·). The experimental data (■) are from Li et al. [14]

using, respectively, the prolate and oblate quadrupole density distributions as provided by Sarriguren [2] which are included in Fig. 1a. The ground state of ^{27}Al has a prolate shape, and ϱ_2(prolate) compares well with the $L = 2$ density distribution from [12]. The oblate density distribution corresponds to an excited state of the ^{27}Al nucleus at a very low energy (0.843 MeV), but for the sake of comparison this excitation energy is neglected and a spin $J_i = \frac{5}{2}$ is assigned like for the prolate ground state (as done in [2]). The evident difference between ϱ_2(prolate) and ϱ_2(oblate) is a difference in sign which plays no role in the cross section as long as the nucleus is unpolarized (see Sect. 2). However, there are also deviations in absolute value and in the position of the extremum which are perceptible in the cross section. As concerns the spherical density distribution ϱ_0, there exist tiny shape dependencies too [2] which, however, are not considered in the present calculations.

In the following, the angular distribution of the scattered electrons and their spin asymmetry are investigated, and subsequently the energy distribution at the cross section minima is examined. Finally the influence of an additional nuclear polarization is considered.

4.1 Angular distribution

Figure 3 shows the angular distribution of the scattered electrons at 250 MeV impact energy. According to Fig. 2a, the quadrupole contribution is only perceptible in the region of the diffraction minima, where the difference between the prolate and oblate shapes can be observed. For unpolarized collision partners the prolate-oblate difference near the scattering angle of $\theta = 64°$ is around 20%. Experiment [14] clearly favours the prolate shape. Note that the error bars are within the size of the symbols.

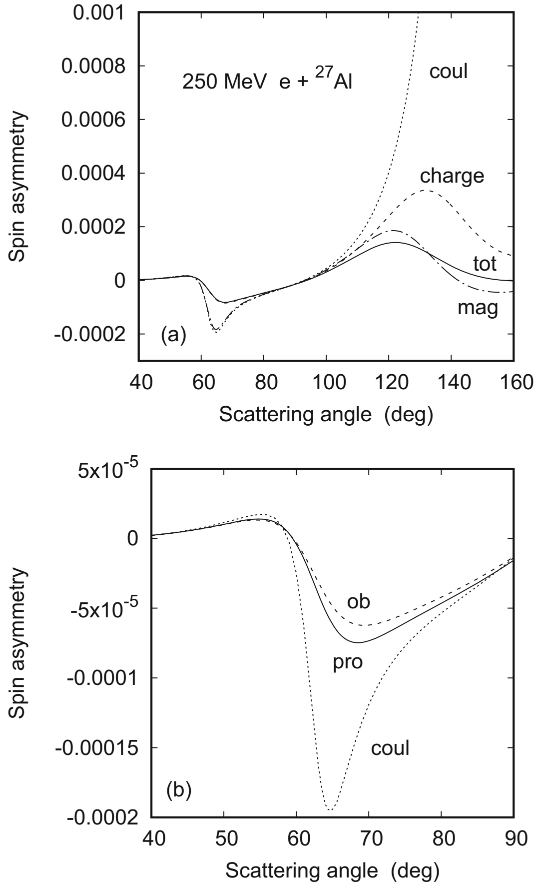

Fig. 4 Angular distribution of the Sherman function S for 250 MeV electrons polarized perpendicular to the beam axis and impinging on ^{27}Al. **a** shows the result when summed over all L (———, using F_2^c from Radhi et al. [12]), when summed over even $L > 0$ (— — ——), when summed over odd $L > 0$ (— · — · —) and for $L = 0$ (· · · · · ·). **b** shows the result when summed over all L, using for F_2^c the prolate density distribution (———), respectively the oblate density distribution (— — ——) from Sarriguren [2]. The angular region covers the first diffraction minimum of $\frac{d\sigma_{\text{coul}}}{d\Omega}$, with a large excursion of the corresponding Sherman function (· · · · · ·)

This shape difference is slightly more pronounced in the case of polarized electrons. The perpendicular spin asymmetry S, also known as Sherman function, is a particularly sensitive parameter. It is the relative difference in intensity when the beam-normal spin of the incoming electron is flipped,

$$S = \frac{\sum_{\sigma_f} d\sigma(\boldsymbol{\zeta}_i, \boldsymbol{\zeta}_f)/d\Omega - \sum_{\sigma_f} d\sigma(-\boldsymbol{\zeta}_i, \boldsymbol{\zeta}_f)/d\Omega}{\sum_{\sigma_f} d\sigma(\boldsymbol{\zeta}_i, \boldsymbol{\zeta}_f)/d\Omega + \sum_{\sigma_f} d\sigma(-\boldsymbol{\zeta}_i, \boldsymbol{\zeta}_f)/d\Omega}. \tag{4.3}$$

The final spin polarization remains unobserved, implying a sum over the respective spin projection σ_f. The advantage of such a polarization measurement is that the experimental

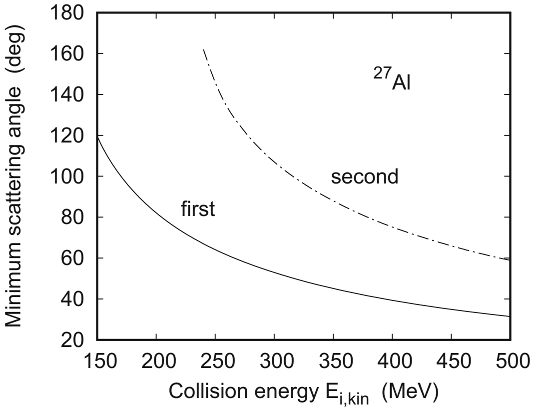

Fig. 5 Position $\theta_{\min}$ of the first (——) and the second ($- \cdot - \cdot -$) diffraction minima as a function of collision energy $E_{i,kin}$ for electrons scattering elastically from ^{27}Al

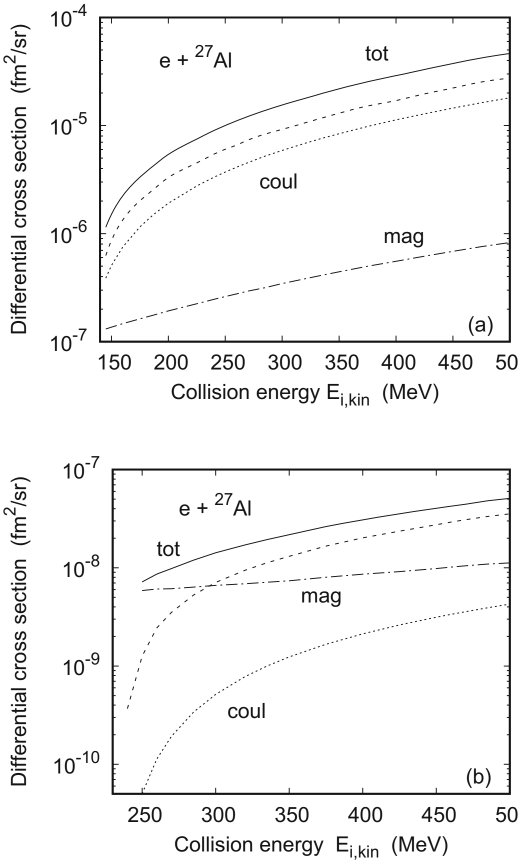

Fig. 6 Differential cross section $\frac{d\sigma}{d\Omega}$ in **a** the first and **b** the second diffraction minimum as a function of collision energy $E_{i,kin}$. Shown is the sum over all L (——), the phase-shift contribution $L = 0$ ($\cdots\cdots$), the charge contribution $L = 2, 4$ (− − − −) and the summed magnetic contribution $L = 1, 3, 5$ ($- \cdot - \cdot -$)

determination of the cross section on an absolute scale is not required.

In Fig. 4a, the angular dependence of the Sherman function is shown for 250 MeV electron impact. When only the spherical part of the nuclear density distribution is considered, S displays resonance structures in the vicinity of the cross section minima, which are particularly pronounced near the second minimum at 146° (where S increases up to 2.3×10^{-3}). These structures are considerably damped when the higher multipoles (both charge and magnetic) are added. The spin asymmetry corresponding to the cross section where all $L \leq 5$ constituents are included, exhibits only flat extrema at the cross section minima.

Figure 4b displays the spin asymmetry for the case of a prolate, respectively oblate, quadrupole contribution in the region of the first diffraction minimum as compared to the $L = 0$ result. It is seen that the prolate configuration leads to a larger asymmetry than the oblate one.

4.2 Energy distribution at the diffraction minima

Figure 5 displays the location of the first and second diffraction minima of the differential cross section for potential scattering as a function of collision energy, $E_{\mathrm{i,kin}} = E_i - c^2$. The second minimum is only clearly visible for energies beyond 240 MeV. Since the momentum transfer $\boldsymbol{q}$ to the nucleus is basically fixed at the diffraction minima, their position decreases with energy, corresponding to the formula $q \approx 2E_i/c\ \sin(\theta/2)$.

The energy dependence of the cross section in the two diffraction minima is depicted in Fig. 6. It is seen that $d\sigma/d\Omega$ increases monotonously with energy. In its first minimum (Fig. 6a) the main contribution is due to the even multipoles with $L > 0$, while the magnetic scattering is unimportant. The cross section at the second minimum (Fig. 6b) is only for energies above 300 MeV dominated by the $L = 2$ (and to a lesser extent $L = 4$) contribution, whereas at low energies the magnetic contribution prevails, basically because of the much larger scattering angles involved (see Fig. 5).

Figure 7 displays the results in the first minimum for the prolate and oblate cases, showing that their difference is approximately constant, irrespective of the beam energy.

In the second minimum this difference is very small at all energies, ranging from 2% at 250 MeV to 7% at 500 MeV, due to the minor importance of the quadrupole charge scattering.

The energy dependence of the spin asymmetry in the diffraction minima is displayed in Fig. 8. Like for the cross section, the deviation between the prolate and the oblate shapes is much larger in the first diffraction minimum than in the second one. And again, for a given minimum, i.e. for a fixed momentum transfer, the prolate-oblate difference is nearly constant in energy. Explicitly (in the first minimum), at 150 MeV, the spin asymmetry is 25% higher for the prolate shape, which decreases to 90% of this value at 400 MeV.

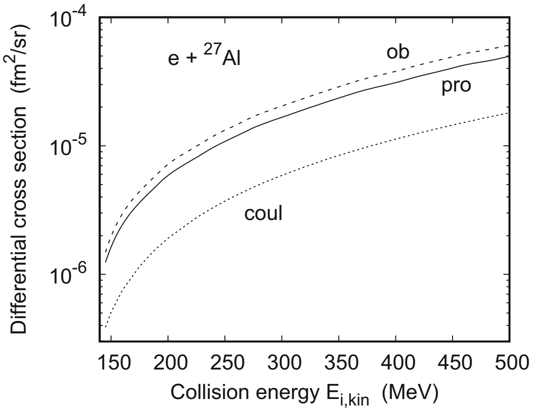

Fig. 7 Differential cross section in the first diffraction minimum as a function of collision energy $E_{i,kin}$. Shown is the sum over all L for the prolate case (———) and for the oblate case (— — ——). Included is the $L = 0$ result from Fig. 6a (······)

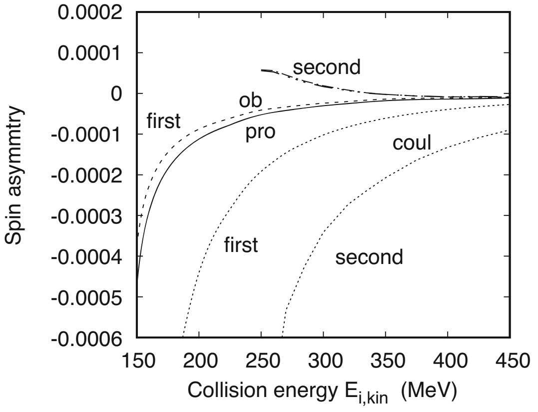

Fig. 8 Sherman function S in the first and second diffraction minima as a function of collision energy. Shown are the results, summed over all L, for the prolate shape in the first (———) and second (— · — · —) minimum, and for the oblate shape in the first (— — ——) and second (— · · · —) minimum. Included is the $L = 0$ result in the first (······, left-hand curve) and second (······, right-hand curve) minimum

4.3 Influence of nuclear polarization

Until now only electron polarization was considered. Here the case is discussed where the target nucleus is in a fixed magnetic substate M_i prior to the collision. This reflects the situation investigated by Sarriguren [2] who considered unpolarized electrons colliding with a target aligned with respect to the direction of momentum transfer. This alignment destroys the incoherence between the contributions from the densities pertaining to a given angular momentum L. In fact, in the above formalism, $\frac{1}{2J_i+1}\sum_{M_i}$ has to be eliminated from (2.1), such that S_{fi} has to be evaluated from the so modified (2.1) with (2.3) and (2.4) without any further simplification. Since (2.8) and (2.9) are no longer applicable, one has no more any restriction on angular momentum L in the interference terms, making all of them nonvanish.

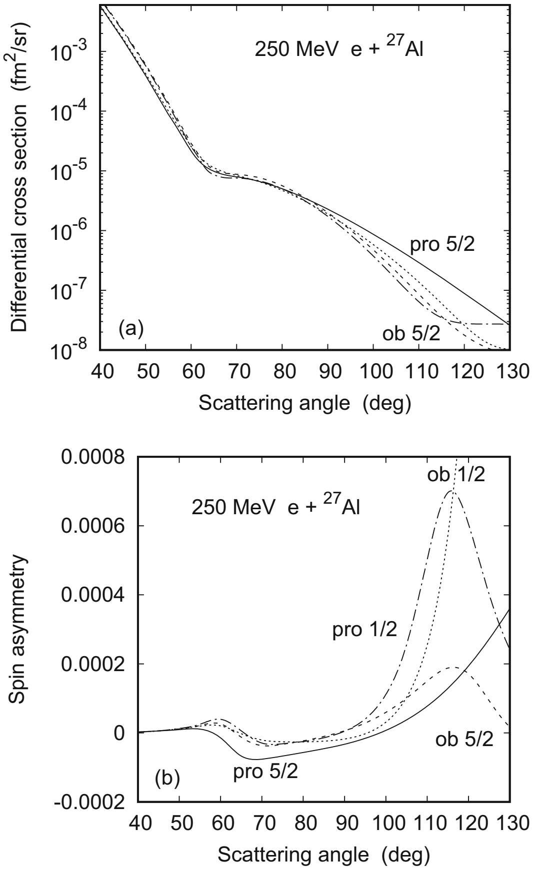

Fig. 9 **a** Differential cross section at 250 MeV for unpolarized electrons and **b** Sherman function for polarized electrons, additionally fixing the nuclear magnetic substate M_i, as a function of scattering angle θ. $M_i = 5/2$: ———, prolate shape; — — ——, oblate shape. $M_i = 1/2$: — · —, prolate shape; ······, oblate shape

This sensitivity to the relative phases between the various angular momentum components enhances the prolate-oblate effect, particularly at large angles. This is demonstrated in Fig. 9a where again a collision energy of 250 MeV has been chosen. Two cases, $M_i = \frac{1}{2}$ and the maximum value $M_i = \frac{5}{2}$, are selected. Whereas the respective shape difference varies between 10 and 40% at angles below 100°, it increases mostly by a factor of 2 ($M_i = \frac{1}{2}$), respectively 3 $\left(M_i = \frac{5}{2}\right)$ for $\theta \gtrsim 110°$.

Figure 9b shows the effect on the electronic spin asymmetry when both electron and nucleus are polarized. The Sherman function is displayed for $M_i = \frac{1}{2}$ and $\frac{5}{2}$ in case of the prolate and oblate nuclear shapes. In contrast to the $M_i = \frac{1}{2}$ state, considerable shape differences are predicted for the $M_i = \frac{5}{2}$ state even near the first diffraction minimum at 64.1° (of a factor of 2 or more). Above 120° where the vicinity of the second diffraction minimum (at 146°) induces large resonance structures in S, there exist extreme prolate-oblate differences for both M_i.

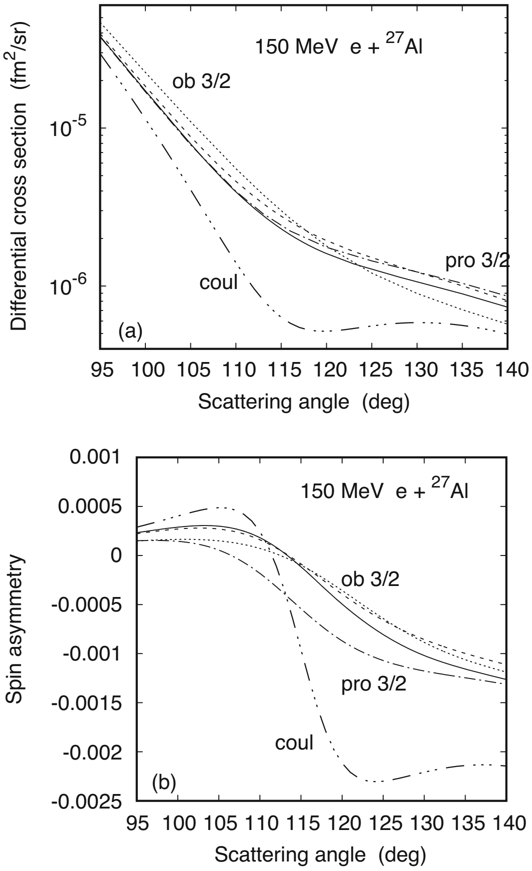

Fig. 10 **a** Differential cross section at 150 MeV for unpolarized electrons and **b** Sherman function for polarized electrons as a function of scattering angle θ. Results are shown for unpolarized nuclei (——, prolate shape; − − − −, oblate shape) and for polarized nuclei with $M_i = \frac{3}{2}$ (— · — · —, prolate shape; · · · · · ·, oblate shape). Also shown is the result from ($L = 0$) potential scattering (— · · · — · · · —)

Figure 10 compares both cross section and Sherman function for polarized and unpolarized nuclei at a lower impact energy of 150 MeV. Here the diffraction minimum is very shallow, and the total cross section decreases monotonously. Clearly, the prolate-oblate difference in the cross section is enhanced when the nuclear polarization is fixed, particularly below and above the diffraction minimum at 119.5°, reaching up to 50% (as compared to the maximum value of 20% for unpolarized nuclei). For the spin asymmetry (Fig. 10b), this enhancement by the polarization of the nucleus is particularly visible at the lower angles, whereas a noticeable prolate-oblate difference exists even for unpolarized nuclei above 130°.

5 Conclusion

Within the DWBA theory we have investigated how the nuclear quadrupole deformation influences the differential scattering cross section for unpolarized electrons and the spin asymmetry for perpendicularly polarized electrons colliding with an ^{27}Al nucleus. The difference between prolate and oblate configurations is basically visible in the first diffraction minimum (i.e. for a momentum transfer $q \approx 1.35$ fm) and amounts, hardly dependent on collision energy, to 20% in the cross section and about 25% in the spin asymmetry. The second diffraction minimum is to a good extent filled by magnetic scattering, such that quadrupole effects, and hence prolate-oblate differences, are suppressed (cross-section differences are around 5%, while spin-asymmetry differences vary between 1 and 10%).

If the spin asymmetry is considered experimentally, a rather low collision energy (say, between 150 and 300 MeV) should be preferred. In this way one can profit from the strong increase of the spin asymmetry with angle at fixed momentum transfer as well as from the near constancy of the prolate-oblate difference when the energy is varied.

An initial spin polarization of the nucleus strongly enhances the prolate-oblate distinction, both in the cross section, as well as in the spin asymmetry of additionally polarized electrons. In particular, there is no longer any correlation between the visibility of the shape differences and the location of the diffraction minima.

The present results, obtained for an aluminum target, are supposed to hold qualitatively also for other nuclei with spin $J_i \geq \frac{3}{2}$. Even in the experimentally simplest case of unpolarized collision partners we have demonstrated that a comparison with the measured cross section can differentiate between nuclear models favouring a prolate or oblate nuclear shape.

Funding Open Access funding enabled and organized by Projekt DEAL.

Data Availability Statement This manuscript has no associated data. [Author's comment: There is no additional data or software code to this manuscript.]

Code Availability Statement This manuscript has no associated code/software. [Author's comment: There is no additional data or software code to this manuscript.]

References

1. B.W. Downs, D.G. Ravenhall, D.R. Yennie, Phys. Rev. **106**, 1285 (1957)
2. P. Sarriguren, Phys. Rev. C **109**, 024312 (2024)
3. H. Überall, *Electron Scattering from Complex Nuclei* (Academic Press, New York, 1971)
4. J.F. Prewitt, L.E. Wright, Phys. Rev. C **9**, 2033 (1974)
5. D.H. Jakubassa-Amundsen, Nucl. Phys. A **975**, 107 (2018)
6. T.W. Donnelly, I. Sick, Rev. Mod. Phys. **56**, 461 (1984)
7. A.R. Edmonds, *Angular Momentum in Quantum Mechanics*, 2nd edn. (Princeton University Press, Princeton, 1960)
8. C.M. Vincent, H.T. Fortune, Phys. Rev. C **2**, 782 (1970)
9. V.A. Yerokhin, A. Surzhykov, Phys. Rev. A **82**, 062702 (2010)
10. H. De Vries, C.W. Jager, C. De Vries, At. Data Tables **36**, 495 (1987)
11. F. Salvat, J.M. Fernández-Varea, W. Williamson Jr., Comput. Phys. Commun. **90**, 151 (1995)
12. R.A. Radhi, A.A. Alzubadi, N.S. Manie, Nucl. Phys. A **1015**, 122302 (2021)
13. G.C. Li, I. Sick, J.D. Walecka, G.E. Walker, Phys. Lett. **32B**, 317 (1970)
14. G.C. Li, M.R. Yearin, I. Sick, Phys. Rev. C **9**, 1861 (1974)
15. L. Lapikás, A.E.L. Dieperink, G. Box, Nucl. Phys. A **203**, 609 (1973)